Large Strain Mechanical Behavior of HSLA-100 Steel Over a Wide Range of Strain Rates

Maen Alkhader
Graduate Aerospace Laboratories,
California Institute of Technology,
1200 E. California Boulevard,
Pasadena, CA 91125-5000;
Mechanical Engineering Department,
Stony Brook University,
Stony Brook, NY 11794-2300
e-mail: maen.alkhader@stonybrook.edu

Laurence Bodelot
Graduate Aerospace Laboratories,
California Institute of Technology,
1200 E. California Boulevard,
Pasadena, CA 91125-5000
e-mail: lbodelot@caltech.edu

High-strength low alloy steels (HSLA) have been designed to replace high-yield (HY) strength steels in naval applications involving impact loading as the latter, which contain more carbon, require complicated welding processes. The critical role of HSLA-100 steel requires achieving an accurate understanding of its behavior under dynamic loading. Accordingly, in this paper, we experimentally investigate its behavior, establish a model for its constitutive response at high-strain rates, and discuss its dynamic failure mode. The large strain and high-strain-rate mechanical constitutive behavior of high strength low alloy steel HSLA-100 is experimentally characterized over a wide range of strain rates, ranging from 10^{-3} s^{-1} to 10^4 s^{-1}. The ability of HSLA-100 steel to store energy of cold work in adiabatic conditions is assessed through the direct measurement of the fraction of plastic energy converted into heat. The susceptibility of HSLA-100 steel to failure due to the formation and development of adiabatic shear bands (ASB) is investigated from two perspectives, the well-accepted failure strain criterion and the newly suggested plastic energy criterion [1]. Our experimental results show that HSLA-100 steel has apparent strain rate sensitivity at rates exceeding 3000 s^{-1} and has minimal ability to store energy of cold work at high deformation rate. In addition, both strain based and energy based failure criteria are effective in describing the propensity of HSLA-100 steel to dynamic failure (adiabatic shear band). Finally, we use the experimental results to determine constants for a Johnson-Cook model describing the constitutive response of HSLA-100. The implementation of this model in a commercial finite element code gives predictions capturing properly the observed experimental behavior. High-strain rate, thermomechanical processes, constitutive behavior, failure, finite elements, Kolsky bar, HSLA-100. [DOI: 10.1115/1.4005268]

1 Introduction

High-strength low alloy steels (HSLA) are finding increasing use in applications involving impact loading and considered as an alternate to widely used high-yield (HY) strength steels. Multiple grades of HSLA steels have been introduced since the 1980's, namely HSLA-65, 80, and 100; however, this study is focused towards HSLA-100. Unlike the former HY steels whose strength and toughness are derived from the formation of quenched and tempered martensite, HSLA steels are low in carbon and their strength and toughness are derived from a combination of ferrite grain refinement and precipitation strengthening [2,3]. With the high content of carbon in HY steels, welding of these steels requires detailed and expensive control on their preheat and post-heat treatment to ensure the production of an adequate microstructure [3]. The overwhelming need for welding to fabricate naval ships and structures renders the use of HY steels very expensive

The characterization of the large strain and high-strain rate response of HSLA-100 steel is a key step towards its accurate utilization in marine and structural applications that might be subjected to impact or high-strain rate loadings. Moreover, to ensure structural integrity, the sensitivity of HSLA-100 steel mechanical behavior to manufacturing processes and microstructure has to be well characterized. For the latter, Das et al. [4] and Dhua et al. [5,6] conducted mechanical and electron microscopy studies to address the coupling between microstructure, processing, manu-

facturing techniques and mechanical properties. Similarly but aiming toward higher strain rates, Xue et al. [7] investigated the dynamic tensile response of HSLA-100 steel near weld zones at strain rates ranging from quasi-static to dynamic (10^3 s^{-1}) regimes. Results of this work illustrated the decline in flow stress near weld zones or in the heat affected zones.

As for any structural material, damage, and failure modes are of particular interest as they limit the carrying load capacity. Chae and Koss [8] characterized void nucleation and damage accumulation due to straining. On the other hand, in the perspective of impulsive loading, the prominent failure mechanism is adiabatic shear band (ASB), which represents a localized shear deformation mode triggered by thermomechanical instability at local defect or material inhomogeneity [9–12]. Regarding HSLA-100, using Kolsky torsion bars apparatus in conjunction with high-speed imaging, Latourte et al. [13] investigated ASB formation at stain rates of the order of 2200 s^{-1}.

Although the above-mentioned data are useful and resulted from elaborate efforts, it is limited to strain rates up to 2000 s^{-1}. However, the fact that this steel is used in naval and marine applications makes it very likely to face extremely higher strain rates. In addition, it is not yet represented by a constitutive model that facilitates its implementation in computer simulations for design and analysis purposes. Furthermore, failure due to ASB formation at high deformation rates is reported to occur, but the propensity of developing ASB at high-strain rates is not well characterized except for rates around 2000 s^{-1}, as reported recently [13].

As a result, this study has three objectives: first, obtain detailed measurements and characterization of the high-strain-rate behavior under a wide range of strain rates (10^{-3} s^{-1}–14,000 s^{-1});

second, represent the measured stress-strain curves by a simple Johnson-Cook type constitutive model; and finally, characterize the failure propensity of HSLA-100 steel due to adiabatic shear band.

In this study, we were able to reach strain rates up to 13,500 s^{-1} by using split Hopkinson pressure bar (SHPB) in conjunction with the shear compression specimen (SCS). This specimen was proposed by Rittel et al. [14] and validated by Dorogoy and Rittel [15,16]. Moreover, it has been used to successfully characterize different materials [17,18]. In the context of ASB, SCS specimens would play a dual role. First, they would enable characterizing the compressive response at strains and strain rates higher than those achievable by SHPB on cylindrical specimens, but more importantly they would provide a simple technique to investigate the propensity for ASB formation [17].

This article is organized as follows: first, the experimental approach, tools and data reduction techniques are presented. This is followed experimental results. Finally, discussion and conclusions are presented, respectively.

2 Experimental Procedure

2.1 Test Protocols and Specimens. Quasi-static tests at a strain rate of 10^{-3} s^{-1} were performed on a hydraulic testing machine (MTS) under displacement control. To minimize any unwanted shear forces on the specimen-loading rod interface, and to ensure the coaxiality of the compressive forces at the specimen interfaces, a compression fixture was used in all quasi-static tests. The history of deformation for all tested specimens was acquired and reported by the testing machine transducer, which was calibrated to account for the machine and fixture compliance. Loading history was reported by the machine load cell, which had a capacity of 220 kN.

Dynamic tests were conducted on a Kolsky (split Hopkinson) pressure bar. The setup had an incident and transmission bars with lengths of 1215 and 1010 mm, respectively. Bars had a common diameter of 19.05 mm and are made of precision ground high-strength C350 maraging steel. Pressure pulse duration was controlled by the length of the striker bar used. The Kolsky pressure bar technique is a well-established high-strain-rate testing technique. The details and history behind this technique can be found elsewhere [19,20].

Two types of specimen were used in this study: cylindrical specimens and SCS. For the cylindrical specimen, two sets were used. One set had a height of 7.6 mm with a diameter to height aspect ratio of 1. A second set had a height of 5 mm with diameter to height aspect ratios of 1, 1.5, and 2. All shear compression specimens have a rectangular shape with identical dimensions, except for the gage width, which had the values of $w = 2.54$, 1.7, and 0.5 mm (see Fig. 1). They will be used for different types of experiments, as explained below.

Quasi-static experiments at a rate of 10^{-3} s^{-1} were performed on the 7.6 mm height cylindrical specimens according to common mechanical tests standards. For comparison purposes and to ensure the accuracy of the stress-strain response measured using SCS specimens, quasi-static tests at a rate of 10^{-3} s^{-1} were performed on SCS specimens with a gage width of 2.54 mm using the same testing machine and under identical conditions and loading rate.

High-strain rate experiments were performed at strain rates ranging from 2×10^3 s^{-1} to 1.35×10^4 s^{-1}. Cylindrical specimens with a height of 5 mm and diameter to height ratios of 1, 1.5, 2 were tested using SHPB to obtain a high-strain rate response up to 4100 s^{-1}. Different aspect ratios were used to achieve the highest strain rate that could possibly be reached with the cylindrical specimens. Above the limit mentioned earlier, the SCS had to be used to achieve higher strain rates. The SCS were used with different values of gage width: $w = 2.54$, 1.7, and 0.5 mm, a narrower gage width leading to higher strain rates. For comparison with the cylindrical specimen, shear compression specimens were also
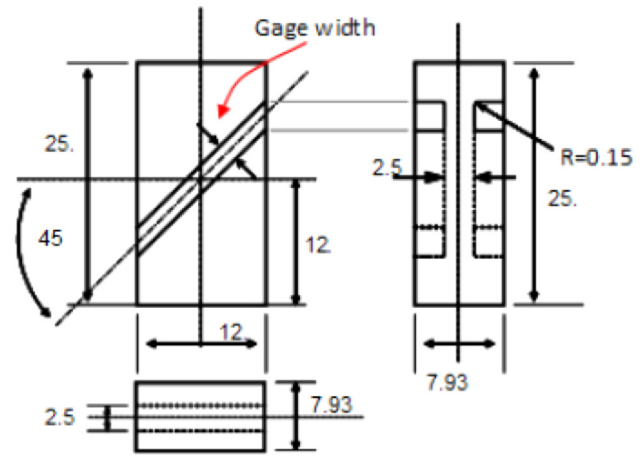

Fig. 1 Geometry and dimensions (mm) of the shear compression specimens

tested at intermediate strain rates of approximately 2000 s^{-1} and 3000 s^{-1}.

Note that, for practical convenience, the investigation of the thermomechanical coupling and the ratio of plastic work converted into heat was only conducted on the cylindrical specimen under dynamic loading.

2.2 Thermomechanical Coupling. Only a fraction of the plastic work performed during plastic deformation of metals is stored in the form of energy of cold work; most of the plastic work is converted into heat which, if not dissipated out of the deformed material, will lead to a temperature increase. For high-strain rates, the process is adiabatic. A rigorous thermodynamically-based proof of the adiabatic assumption during high-strain rate deformation can be found in Ref. [21].

For structural design and reliability purposes, accurate prediction of temperature increase is important especially for materials susceptible to thermal softening and failure due to adiabatic shear bands. Temperature increase during adiabatic high-strain rate loading due to plastic deformation can be predicted once the fraction of plastic work converted into heat, β, is separated from the stored energy of cold work. Accordingly, β, can be defined as [21]

$$\beta = \frac{\rho c_p \dot{T}}{\sigma_{ij} \dot{\varepsilon}_{ij}^p} = \frac{\dot{Q}}{\dot{W}^p} = \frac{dQ}{dW^p} = \frac{\rho c_p dT}{\sigma_{ij} d\varepsilon_{ij}^p} \qquad (1)$$

such that Q is the thermal dissipation and W^p is the plastic work exerted to deform the specimen. Temperature, stress and strain inside the specimen are recorded simultaneously during the experiment to compute the value of the parameter β, and to describe its evolution during the deformation history as a function of both accumulated plastic strain and strain rate.

The experimental technique adopted in this study is identical to the one used in the work of Rittel et al. [22]. The infrared temperature measurement system utilized a single high-speed HgCdTe detector with its appropriate amplifier (Judson PA-100). A 1X reflective Newtonian optical system consisting of parabolic mirrors with a radius of curvature of 70 mm and a flat mirror oriented at 45deg are used to focus the infrared (IR) radiation on the detector. Figure 2 illustrates the temperature measuring system. The detector has an active area of 100×100 μm^2 and is placed in a liquid nitrogen cooled Dewar to maximize its sensitivity and its signal-to-noise ratio at temperatures close to room temperature. Details about alignment of the system and its calibration can be found in Ref. [22].

2.3 Data Reduction for the Shear Compression Specimen. The shear compression specimen developed by Rittel et al. [14] not only extends the range of the strain rates achievable by Kolsky
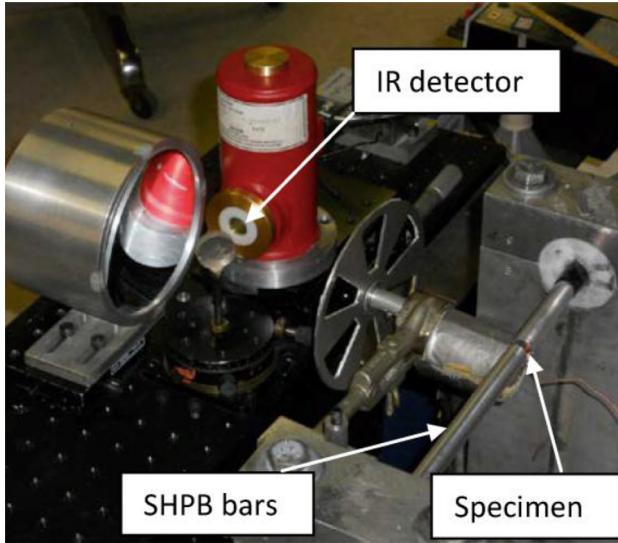
Fig. 2 Infrared detector and optical system integrated with SHPB

Fig. 3 Quasi-static stress-strain response of HSLA-100 at a strain rate of 10^{-3} s^{-1}

Table 1 SCS fitting parameters

Gage width (w)	2.54 (mm)	1.7 (mm)	0.5 (mm)
K_1	0.975	0.930	0.901
K_2	0.212	0.220	0.230
K_3	0.9332	0.8284	0.564

bar setup, but it also subjects the gage section of the specimen to a shear dominant state of stress. The von Mises stress and equivalent strain fields within the gage section can be determined using the following empirical equations, as suggested by Rittel et al. [23]

$$\varepsilon_{eq} = K_3 \frac{d}{h}; \quad \dot{\varepsilon}_{eq} = K_3 \frac{\dot{d}}{h} \tag{2}$$

$$\sigma_{eq} = K_1 \left(1 - K_2 \varepsilon_{eq}\right) P/Dt \tag{3}$$

such that, d is the prescribed displacement applied at the specimen interface, h is the gage height, P is the applied load, D is the specimen width, t is the gage thickness, K_1, K_2, and K_3 are constants whose values are to be found by fitting the empirical equations with data obtained from finite element (FE) analysis [14,17,23]. Detailed FE analysis was thus performed on the SCS specimens used in this study to obtain the most appropriate constants for each gage width. The analysis implemented the quasi-static plastic response obtained from testing cylindrical specimens. Table 1 presents the constants obtained from FE analysis. The accuracy of the obtained constants was confirmed by the observed good fit between cylindrical and SCS specimen results.

3 Results

3.1 Quasi-Static Response. Results from the quasi-static tests conducted at a strain rate of 10^{-3} s^{-1} are presented in Fig. 3. Both SCS and cylindrical specimens result in identical true stress-strain compressive response as illustrated in Fig. 3, where the responses from two identical cylindrical specimens are plotted to enlighten repeatability. The bilinear hardening response visible in Fig. 3 is used in the finite element simulations to obtain the empirical constants for the SCS specimens.

3.2 High-Strain Rate Stress-Strain Response. The true stress-strain curves representing the flow stress for HSLA-100
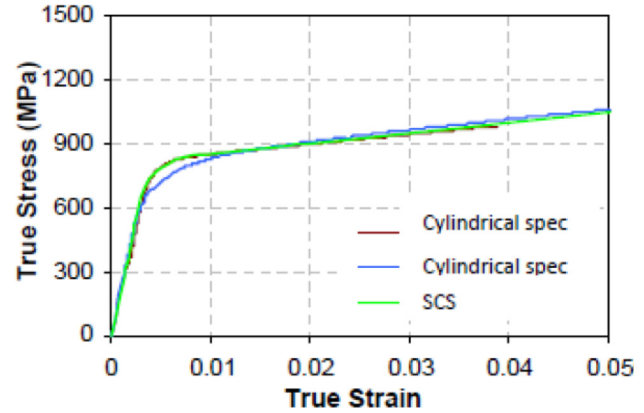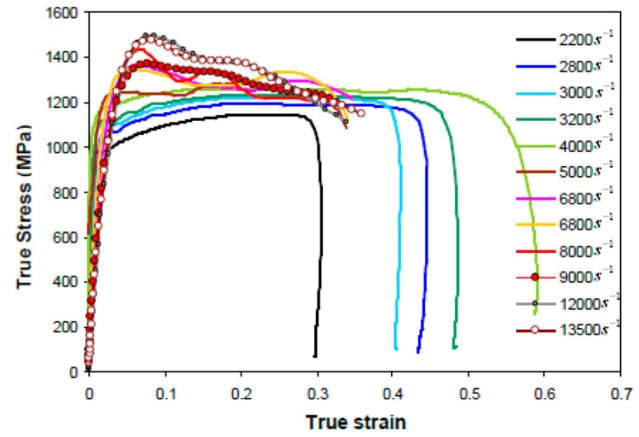

Fig. 4 Stress-strain response of HSLA-100 steel for strain rates ranging between 2200 s^{-1} and 13,500 s^{-1}. Results above 4000 s^{-1} are obtained on SCS specimens.

steel were determined over a wide range of strain rates and are presented in Fig. 4. This figure shows the strong dependence of the flow stress on strain rate, which is a well-established behavior of steel in general [24]. In Fig. 4, flow stress curves for rates exceeding 4000 s^{-1} were obtained by using exclusively SCS specimens with Kolsky bars.

The corresponding flow stress curves, presented in Fig. 4, are limited by the failure strain due to the formation of adiabatic shear bands. The onset of failure due to shear band formation in the gage section of SCS specimens is determined by the appearance of a discontinuity and a sudden increase in the strain rate history defined by Eq. (2) as will be illustrated in the discussion (Sec. 4). Strain rate discontinuity results from a sudden drop in the transmitted strain signal as the gage section loses its load carrying capacity due to the formation of an adiabatic shear band.

At the intermediate strain rates of 3000 and 4000 s^{-1}, true stress-strain curves were obtained from both cylindrical and SCS specimens and are plotted together in Fig. 5 to allow for a clearer comparison. This figure confirms that there is a good degree of agreement between the results obtained from SCS and cylindrical specimens. Since loading rates beyond 4000 s^{-1} were only attainable by using SCS specimens, no comparison with cylindrical specimens results are possible. However, the comparison made in Fig. 5 is sufficient to prove that switching specimen geometry to enable higher strain rates does not affect the results, as demonstrated also by Vural et al. [17].

Although the flow curves of Fig. 4 represent the general material behavior at various strain rates, particular interest lies in some key quantities that can be extracted from these flow curves, such
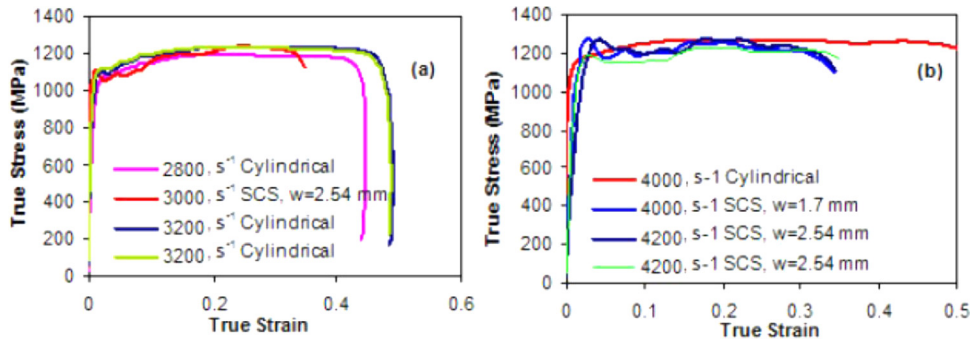
Fig. 5 Stress-strain response of HSLA-100 steel as obtained from cylindrical and shear compression specimens for two strain rates ranges: (*a*) 3000 s^{-1} and (*b*) 4000 s^{-1}
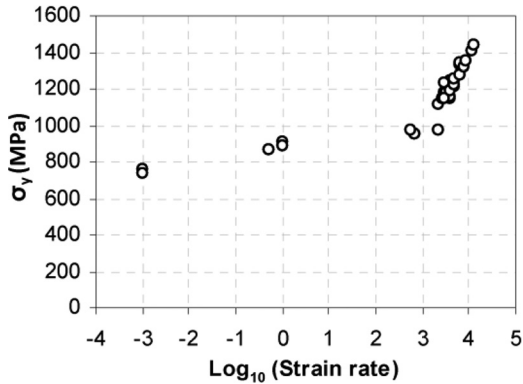

Fig. 6 Flow stress at 0.1 plastic strain as a function of strain rate

Fig. 7 Evolution of the fraction of plastic work converted into heat β with strain and strain rate for HSLA-100 steel

as initial yield point, hardening rate and softening driven by strain rate. Initial yield stresses taken at 0.1 plastic strain were extracted from the flow stress curves of Fig. 4 and are plotted in Fig. 6. Significant initial yield stress enhancement with increased strain rate can be clearly observed from Fig. 6. As a matter of fact, the measured initial yield strength expressed as a function of the logarithmic value of strain rate exhibits a bilinear behavior, with a change of slope occurring for a strain rate of 1000 s^{-1} (corresponding to a logarithmic value of 3). Similar bilinear behavior has been observed before as illustrated in the comparison included in Ref. [25] for 99.99% pure iron, Mild steel and 99.6% pure steel. Conversely, as seen in Fig. 4, the rate of strain hardening follows a different pattern; hardening rate decreases with increasing strain rate, while stress softening is observed at strain rates above 6000 s^{-1}. The extreme softening observable at the highest rates is influenced by strain localization at the gage boundaries due to the significant change in specimen geometry. Such localization is accompanied by higher strain rates and elevated temperatures, which promote thermal softening and result in an adiabatic shear band. Thus, care should be taken while interpreting flow stresses resulting from SCS specimens at large strains and very high-strain rates.

3.3 Thermomechanical Coupling. Results for the fraction of plastic work converted into heat, β, measured from the adiabatic high-strain-rate tests performed on the cylindrical steel specimens are presented in Fig. 7. This figure shows the evolution of β with strain at various strain rates, covering the range attainable with the cylindrical specimens. Curves representing the evolution of β illustrate a similar trend: generally, the value of beta increases linearly from around 0.65 until it saturates to a value of 0.9 at a plastic strain value of 0.2, after which, β tends to remain steady at a plateau value of 0.9 with further plastic strain. Occasionally, stress wave reverberations within the specimen might
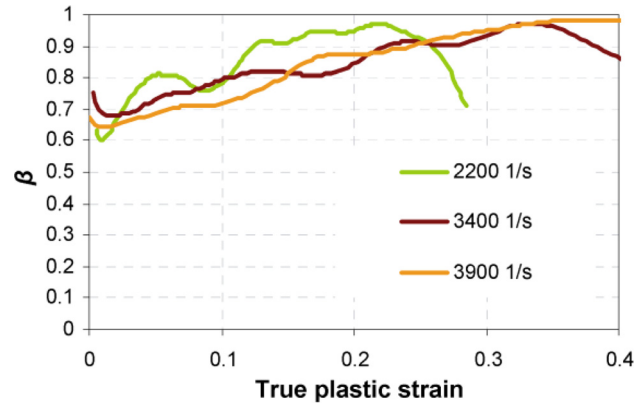
cause it to move slightly out of the focus plane, which would lead to a pronounced drop in the measured value of β, similar to the drop in the curve presenting β at a strain rate of 2200 s^{-1}. Based on the aforementioned results, one can generally say that almost 90% of the plastic work energy is dissipated into heat, which leads to a significant increase in the temperature of the specimen as the deformation process is adiabatic.

3.4 Johnson-Cook Constitutive Model. As HSLA steels are primarily used in fabricating large naval structures, it is important to establish a simple computationally well-suited constitutive model to predict the large strain and high-strain rate behavior of such steels. The phenomenological Johnson-Cook model [26] is favored in this study over physically based models due to its simplicity and availability in most commercial finite element codes. The J-C model combines the effects of strain, strain rate and temperature in a multiplicative manner as follows:

$$\sigma_{eq} = (\sigma_0 + B\varepsilon^n)\left(1 + C\ln\frac{\dot{\varepsilon}}{\dot{\varepsilon}_o}\right)\left[1 - \left(\frac{T - T_r}{T_m - T_r}\right)^m\right] \quad (4)$$

such that σ_{eq} is the effective or Mises stress, while ε, $\dot{\varepsilon}$, and T are the strain, strain rate and temperature variables. T_m and T_r are the melting and reference temperatures, respectively. σ_0, B, C, as well as the exponents n and m, are the parameters of the J-C model. σ_0 is the yield stress, B and n represent the effects of strain hardening, C is the strain rate constant and m is linked to the thermal softening.

Stress-strain curves presented in Fig. 4 were used to determine the fitting parameters that would enable Eq. (4) to effectively represent the experimentally obtained results over the wide range of tested strain rates (10^{-3} s^{-1}–13,500 s^{-1}). It should be noted that all experiments were conducted at room temperature; hence, the

Table 2 Johnson-Cook fitting parameters

Parameter	σ_0 (MPa)	B (MPa)	n	C	$\dot{\varepsilon}_0$	T_m (°C)	T_r (°C)	M
For $\dot{\varepsilon} < 1000$ s^{-1}	736	1500	0.505	0.041	0.001	1773	300	1.00
For $\dot{\varepsilon} > 1000$ s^{-1}	920	250	0.66	0.17	1000	1773	300	0.95

only temperature included in the J-C model is the one resulting from the plastic energy converted into heat during the adiabatic deformation. Figure 6 illustrates the existence of two strain-rate-dependent regimes. Both can be considered linear in terms of the logarithmic value of strain rate. At 1000 s^{-1} strain rate sensitivity is increased as evidenced in the increase of the slope. Due to this bilinear relation, J-C model was fitted using two reference strain rates, at 10^{-3} s^{-1} and 1000 s^{-1}. The fitting process commences by determining the values of σ_0 and B through fitting J-C to stress-strain data obtained at the reference strain rate, to exclude the effect of the bracket with the C constant. This was followed by an iterative process to find the values of C and m that enable J-C model to accurately represent the experimental data. An initial estimate for the value of C is found by fitting the data presented in Fig. 6 to two linear lines whose slope can be used as an initial guess for C. On the other hand, the value for m is chosen to be around 1.0, which is a commonly used value for various types of steel [9,26]. The fitting process resulted in the two sets of fitting parameters listed in Table 2: one set of fitting parameters is obtained for strain rates smaller than 1000 s^{-1} while the other is for rates larger than 1000 s^{-1}.

An evaluation of the experimentally obtained Johnson-Cook model is made by comparing the structural response computed numerically with the experimental data obtained from the SHPB tests performed on SCS specimens at the strain rates of 4000 s^{-1}, 6600 s^{-1}, and 13,500 s^{-1}. Simulations were performed using the explicit solver from the commercial finite element software ABAQUS. The Johnson-Cook model from the software built-in material library in conjunction with the parameters listed in Table 2 was used to model the steel response. The deformation process was assumed to be adiabatic as the deformation time span (120 μs) is significantly small for any heat transfer or heat loss to occur. The only source of temperature increase is the fraction of plastic work converted into heat during the adiabatic deformation process. The β parameter was given the value of 0.9 since in ABAQUS the β

parameter is implemented as a strain and strain rate independent material constant. The value 0.9 is usually the one chosen in models taking into account thermomechanical couplings [27].

The FE models are identical in terms of geometry and dimensions to the experimentally tested specimens. To reduce computational cost, symmetry is invoked and only one half of the SCS specimen is included in the FE model. The outer parallelepiped volume which is subjected to an approximately uniform strain field is meshed with linear strain hexagonal eight-noded elements having an average size of 0.4 mm. In the gage area, which is the zone of interest and the region encompassing large plastic deformation, the mesh is refined and comprises elements with a size of 30 μm near the gage edges, while in the center of the gage area elements have a size ranging from 30 μm to 120 μm. The fine mesh near the edges is necessary to accommodate strain gradients due to the change in cross section. Loads were applied as prescribed velocities and displacements; the specimen's top face is loaded with a prescribed velocity representative of the experimental loading, while the opposite face is fixed. Both faces were assumed to be frictionless. A symmetry boundary condition is enforced by restricting the out-of-plane deformation of the nodes lying on the plane of symmetry. For all high-strain-rate simulations, the explicit solver is utilized along with the adiabatic option, which allows temperature to increase due to the plastic energy converted into heat.

For each of the simulated experiments, velocity profiles at the loaded faces of the specimen were extracted from experimental results and the relative velocity between the two ends of the specimen was used to define the idealized relative velocity profile. The idealized relative velocity profiles were then applied as prescribed boundary conditions on the FE models. For all simulated strain rates, each prescribed velocity profile comprised two phases: an initial constant acceleration phase which is followed by a constant velocity phase. To simplify the modeling process, the relative velocity profile was prescribed at one end of the sample while the other end was fixed in space.

Loading forces acting on the SCS specimens during experiments and simulations were extracted and plotted in Fig. 8 as a function of time for strain rates of 4000 s^{-1}, 6600 s^{-1}, and 13,500 s^{-1}. The comparisons made in this figure show the good agreement between the experimental and computational loading force histories. For small to moderate strain rates, Figs. 8(a) and 8(b) illustrate the ability of the simulations to provide accurate
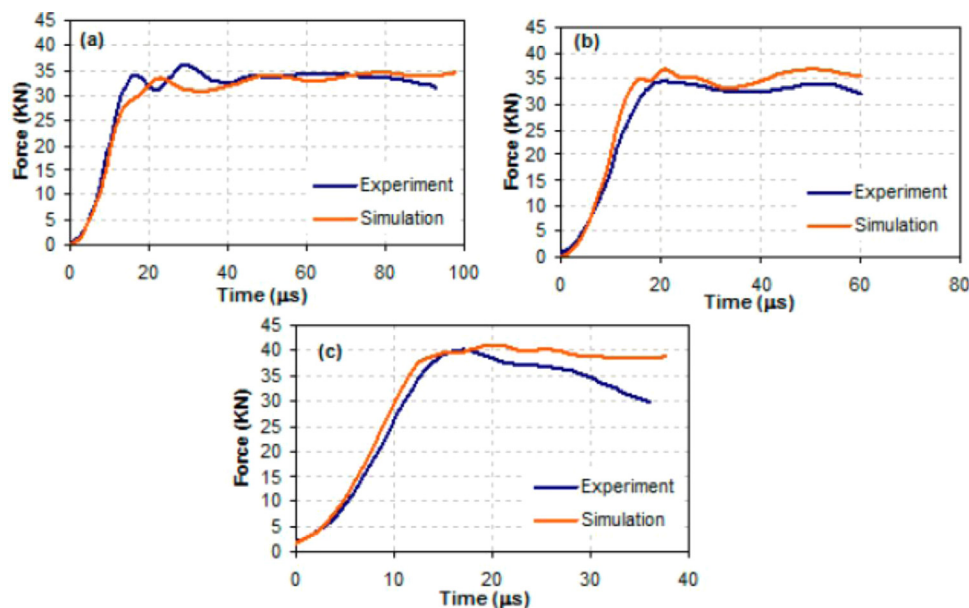

Fig. 8 Force evolution with time during the deformation of HSLA-100 steel SCS specimens at strain rates of (a) 4000 s^{-1}, (b) 6600 s^{-1}, and (c) 13,500 s^{-1}
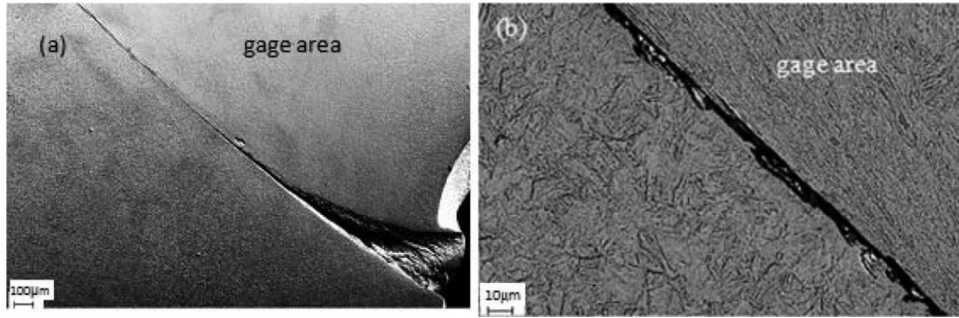
Fig. 9 SEM image of the localized shear band for a shear compression specimen loaded at a strain rate of 5000 s^{-1}, showing (*a*) the gage section and the undeformed region and (*b*) a closer view revealing the texture of the shear band and the undeformed zone

predictions for the variation of force with time during the early stages of deformation as well as at large strains. However, at very high-strain rates (13,500 s^{-1} in Fig. 8(*c*)), the numerically computed force deviates from its measured counterpart at large strains, specifically during the highly localized shear driven softening phase. To further improve the accuracy of the computed force history at very high-strain rates and large strains, refined models with adaptive meshing capabilities as well as damage evolution algorithms should be implemented in the simulations to address shear strain localization and failure. In addition, though the Johnson-Cook model is often used to predict the early stages of the deformation, it is worth mentioning that it does not describe the strain rate sensitivity of the failure strain. As found by Ref. [28], the dependence of failure strain on strain rate is linked to the crystallographic structure of the material and a proper description of the phenomenon would require implementing models tackling with dislocation dynamics.

4 Discussion

4.1 Strain-rate Sensitivity of HSLA-100. Over the entire range of strain rates investigated in this study, results confirm the general trend observed in many metallic and steel materials, where the flow stress increases with strain rate as discussed by Meyers [24]. This effect can be clearly observed in Fig. 6 where flow stress is plotted against the logarithmic strain rate and exhibits a bilinear relationship with a change of slope around 1000 s^{-1}. These results give a new insight into the high-strain rate behavior of HSLA-100 as most of past studies were investigating shear strain rates up to 2200 s^{-1} [13]. In Fig. 6, the flow stress values strictly represent the flow stress at 0.1 plastic strains. Extending the same trend to larger strains may not be accurate as the hardening rate is temperature dependent, which is bound to increase due to the transformation of a fraction of the plastic work into heat during the adiabatic high-strain rate deformation process. At 0.1 plastic strain, the amount of plastic work is insignificant and the corresponding temperature increase and thermal softening would have a minimal effect (see Fig. 7).

4.2 Adiabatic Shear Banding in HSLA-100

4.2.1 Postmortem Observations. All tested cylindrical specimens were severely deformed but all maintained their uniform cylindrical shape and failure in terms of visible crack was not observed. However, failure due to the formation of an adiabatic shear band was observed to occur at the root of the fillet in the inclined gage area (because of the stress concentration promoted by the sudden change in geometry) in most tested SCS specimens, for strain rates above 3000 s^{-1}.

The developed shear bands were investigated using scanning electron microscopy (SEM) on metallographic longitudinal sections of selected SCS specimen. For the specimens studied in the metallographic analysis, stop rings similar to the ones utilized by

Vural et al. [17] were used during dynamic loading to prevent the deformation of the SCS specimens beyond a predetermined strain level (0.35) and to forestall catastrophic failure due to adiabatic shear banding. Prior to observation, the specimen were polished and etched with 2% Nital. Figure 9(*a*) shows the microstructure of a SCS specimen that has been loaded at a strain rate of approximately 5000 s^{-1}. This figure shows a well-defined highly localized shear band running across the specimen and separating the gage section from the remainder of the specimen. It is worth noting that the shear band was not observed on longitudinal sections close to the specimen longitudinal midsection but on longitudinal planes closer to the exterior surface. This illustrates that localization starts near the groove edges due to stress concentration resulting from sudden change in geometry. Then, localization grows deeper (along the normal to the surface) inside the gage area.

Figure 9(*b*) shows a closer view of the fractured shear band which has a width smaller than 10 μm. Outside the gage section and away from the shear band, the material is essentially in its original state, while within the gage section the material has deformed rather homogeneously, as can be noted from the aligned microstructural pattern. The deformation within the shear dominated gage area is aligned with the shear band and the 45 deg gage direction.

4.2.2 Analysis of Shear Bands Formation. Finite element simulations equipped with the Johnson-Cook model (see Sec. 3.4) were utilized to predict localization zones for multiple specimens but, for illustration purposes, focus is limited to the SCS specimen tested at a strain rate of 6600 s^{-1}.

Plastic strain fields obtained at an average gage plastic strain of 0.3 are presented in Fig. 10(*a*). In this figure, the plastic strain contours provide a good prediction for the location and profile of the formed adiabatic shear band. Moreover, a significant temperature rise due to heat generated during the adiabatic deformation
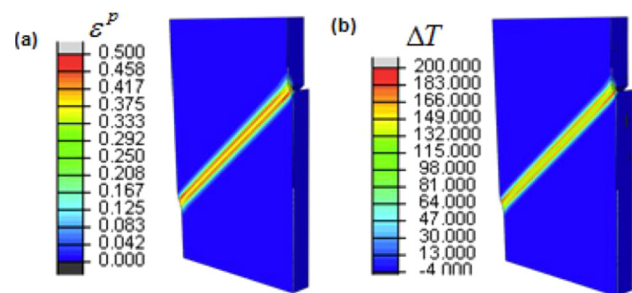

Fig. 10 Case of a SCS specimen with a gage width of 0.5 mm tested at a strain rate of 6600 s^{-1}. (*a*) The plastic strains and (*b*) the temperature distribution are obtained, respectively, at a plane lying 0.2 mm parallel to the groove traction free surface. These contours show significant strain localization whilst the average plastic strain in the gage area is 0.3.
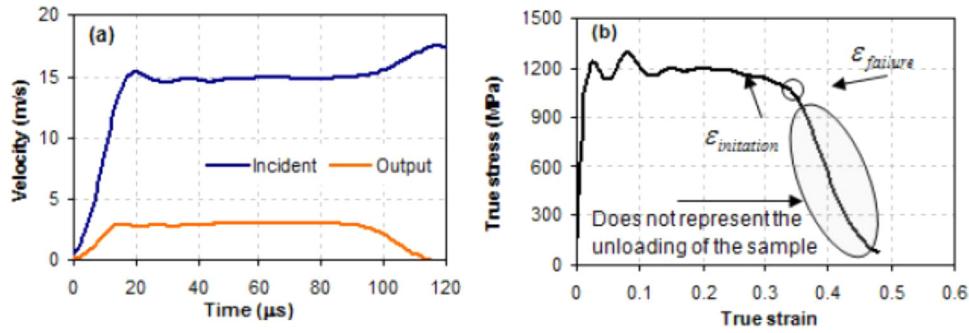
Fig. 11 Loading history observed for a SCS specimen tested at 4000 s⁻¹ strain rate, showing (a) the velocity profiles at the ends of the specimen and (b) the stress-strain response measured during the test
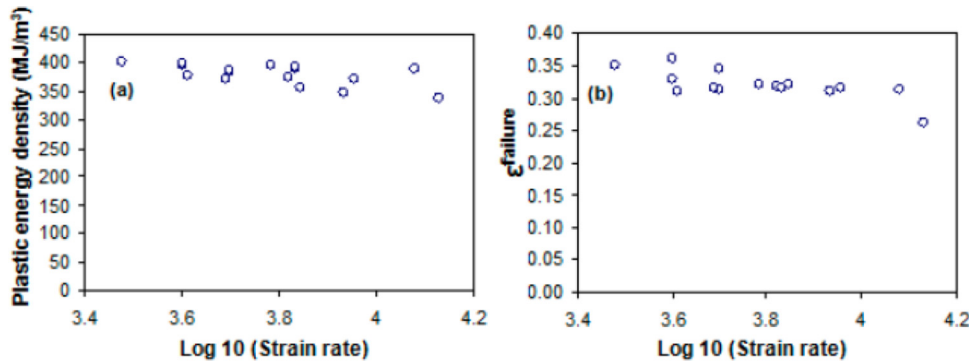

Fig. 12 (a) Plastic energy density and (b) failure strain at the onset of failure due to shear band formation. Both quantities variations are expressed in function of the strain rate.

process coincides with the predicted localized zones, as seen in Fig. 10(*b*). This figure shows that, even as the gage area has a nominal temperature increase around $\Delta T = 80\,°C$, temperature increased by more than $\Delta T = 200\,°C$ at the localized zones. It should be noted that the reported temperature increase from the FE analysis could be a lower bound, as the smallest element used is 3 times the size of the developed shear band and the model didn't incorporate damage evolution and fracture as they are not well documented for the studied steel. Here, mesh refinement was restricted due to computational cost.

Following the idea of unstable plastic deformation proposed by Drucker [29], which is identical to the criterion of maximum effective stress overviewed by Bai and Dodd [9], one can consider the instant at which thermal softening begins to outweigh strain and strain-rate hardening as the initiation moment of ASBs. Beyond this point, localization continues until either the load is removed or a fracture emerges at the localized zone. By ignoring strain, strain rate and temperature history, the maximum shear stress criterion can be used in conjunction with Johnson-Cook model to define the ASB initiation strain (ε_i), simply by solving for the strain satisfying

$$d\sigma_{\text{eff}} = \left(\frac{\partial\sigma_{\text{eff}}}{\partial\varepsilon}\right)_{\dot{\varepsilon},T} d\varepsilon + \left(\frac{\partial\sigma_{\text{eff}}}{\partial\dot{\varepsilon}}\right)_{\varepsilon,T} d\dot{\varepsilon} + \left(\frac{\partial\sigma_{\text{eff}}}{\partial t}\right)_{\dot{\varepsilon},\varepsilon} dT = 0 \quad (5)$$

Solving this equation with the help of the Johnson-Cook model defined by Eq. (4), the ASB initiation strain, ε_i, is found to be approximately 0.265 for the strain rates in the range of 3000–7000 s⁻¹. Higher strain rates might slightly reduce the ASB initiation strain value. This theoretical prediction can be seen to correspond relatively well to the experimentally obtained stress-strain curves at moderate strain rates (see Fig. 4). However, as fluctuations in stress-strain curves due to reverberating stress waves increase

dramatically at higher strain rates, an ASB initiation strain value becomes harder to define experimentally, rendering comparison with theoretical predictions nearly unfeasible. Hence, a more convenient criterion than the maximum shear stress or "initiation" criterion should be investigated.

Another approach to characterize the susceptibility of materials to failure due to ASB is based on identifying the failure strain at which the material loses all its load carrying capacity. Such an approach results in higher strains than those obtained using the maximum stress criterion as significant softening precedes the onset of failure. Failure strains for the tested SCS specimens can be observed in Fig. 4, as curves were terminated at the onset of failure. Since the onset of failure cannot be observed visually during the test, it was established by monitoring the velocity profile at the two faces of specimens. Figure 11(*a*) illustrates such plots for the specimen tested at a strain rate of 4000 s⁻¹. It can be seen that around 90 μs a sudden decrease in the velocity measured from the output bar and an increase in the velocity measured from the incident bar. Such a trend is expected to occur when the incident compressive stress wave cannot be transmitted through the sample, due to the total loss of the specimen load carrying capacity. The state of stress and strain at 90 μs can be seen in Fig. 11(*b*). The 90 μs corresponds approximately to a strain value of 0.35, which is highlighted as the failure strain value $\varepsilon_{\text{failure}}$. It can thus be seen that beyond this point, unloading occurs by a slope that does not represent unloading in the specimen; hence, the part of the curve beyond the failure strain should be ignored. With this criterion, the failure strain is easier to establish but this criterion is not universal in the sense that the failure strain varies with the strain rate, as will be shown in the following paragraph and in Fig. 12(*b*).

Once the failure strain is identified, quantitative insight into the conditions associated with the onset of failure can be gained by calculating the energy of plastic work consumed in deforming the

specimen up to failure (i.e., the area under the equivalent stress-strain curves), as well as, measuring the equivalent plastic strain at the onset of failure $\varepsilon_{failure}$. The energy of plastic work calculated here is similar to the concept of dynamic plastic energy proposed by Rittel et al. [1]. Plastic work results are plotted against the applied strain rates in Fig. 12(a). The data in this figure are obtained from specimens with different gage widths which were subjected to different strain rates; however, the calculated plastic work data approximately follow a constant value, indicating the existence of an energy limit at which the material forms ASB [1]. For comparison, the measured failure strain results are presented in Fig. 12(b) where it can be observed that the failure strain drops slightly with increasing strain rate. Though the drop is not significant enough to recommend excluding the arguments suggesting the existence of a critical failure strain, the energy criterion seems a better candidate to predict failure by adiabatic shear banding in a more robust manner.

5   Conclusions

The large strain constitutive behavior of high-strength low alloy steel (HSLA-100) has been characterized for a wide range of strain rates, ranging from 10^{-3} s^{-1} to 1.35×10^4 s^{-1}, using SHPB and the SCS technique. Conclusions drawn from this study include:

(1) Flow stress at the initial stages of plastic deformation shows a monotonic increase with increasing strain rate. However, at rates exceeding 4000 s^{-1}, the apparent hardening rate decreases with accumulated plastic strain and even becomes negative.

(2) Thermomechanical behavior of HSLA-100 steel was investigated using a high-speed infrared detector in conjunction with SHPB. During adiabatic dynamic deformation, the thermoplastic heat generation was measured and the fraction of plastic work converted into heat, β, was characterized as a function of strain. It is observed that the β factor increases from around 0.65 at early stages of plastic deformation and saturates around a value of 0.9 with further plastic deformation.

(3) Stress-strain curves measured for HSLA-100 were independent of specimen geometry (i.e., SCS or cylindrical) in the common strain rate range attainable by both geometries. At higher strain rates elaborate effort is needed to extend the strain rate range achievable with cylindrical specimens before a comparison can be viable.

(4) A Johnson-Cook model was used to describe the constitutive response of HSLA-100 steel and the relevant parameters were determined from experiments. Validation of the model and the associated parameters was performed using FE simulations. Models in simulations had their geometry identical to the tested SCS specimens. Moreover, loading conditions were extracted from experiments and applied to the models. Great agreement between simulations and experimental results were observed.

(5) Finite element simulations predicted successfully the locality and profile of strain localization and its associated localized temperature increase, which would precede the formation of ASB.

(6) Susceptibility of HSLA-100 steel to ASB formation was assessed by investigating three parameters: initiation strain which represents the maximum shear stress after which the plastic deformation is unstable; failure strain at which the material loses its load carrying capacity and the energy absorbed up to failure which is referred to as dynamic deformation energy. The initiation strain predicted from the Johnson-Cook model was around 0.265 which was observable in some of the experiments. The measured failure strain decreased slightly with increasing strain rate, from 35% to around 30%. The measured dynamic deformation

energy was relatively invariable with variation in strain rates, hence, making it a more suitable and robust quantitative measure of the susceptibility to ASB formation.

References

[1] Rittel, D., Wang, Z. G., and Merzer, M., 2006, "Adiabatic Shear Band Failure and Dynamic Stored Energy of Cold Work," Phys. Rev. Lett., 96(7), p. 075502.
[2] Militzer, M., Hawbolt, E. B., and Meadowcroft, T. R., 2000, "Microstructural Model for Hot Strip Rolling of High-Strength Low-Alloy Steels," Metall. Mater. Trans. A, 31(4), pp. 1247–1259.
[3] Moon, D. W., Fonda, R. W., and Spanos, G., 2000, "Microhardness Variations in HSLA-100 Welds Fabricated With New Ultra-Low-Carbon Weld Consumables," Welding J., 79(10), pp. 278–285.
[4] Das, S. K., Sivaprasad, S., Das, S., Chatterjee, S., and Tarafder, S., 2006, "The Effect of Variation of Microstructure on Fracture Mechanics Parameters of HSLA-100 Steel," Mater. Sci. Eng. A, 431(1–2), pp. 68–79.
[5] Dhua, S. K., Mukerjee, D., and Sarma, D. S., 2003, "Influence of Thermomechanical Treatments on the Microstructure and Mechanical Properties of HSLA-100 Steel Plates," Metall. Mater. Trans. A, 34(2), pp. 241–253.
[6] Dhua, S. K., Mukerjee, D., and Sarma, D. S., 2003, "Effect of Cooling Rate on the as-Quenched Microstructure and Mechanical Properties of HSLA-100 Steel Plates," Metall. Mater. Trans. A, 34(11), pp. 2493–2504.
[7] Xue, Q., Benson, D., Meyers, M. A., Nesterenko, V. F., and Olevsky, E. A., 2003, "Constitutive Response of Welded HSLA 100 Steel," Mater. Sci. Eng. A, 354(1–2), pp. 166–179.
[8] Chae, D., and Koss, D. A., 2004, "Damage Accumulation and Failure of HSLA-100 Steel," Mater. Sci. Eng. A, 366(2), pp. 299–309.
[9] Bai, Y., and Dodd, B., 1992, Adiabatic Shear Localization: Occurrence, Theories and Applications, Pergamon Press, Oxford.
[10] Duffy, J., and Chi, Y. C., 1992, "On the Measurement of Local Strain and Temperature During the Formation of Adiabatic Shear Bands," Mater. Sci. Eng. A, 157(2), pp. 195–210.
[11] Hartley, K. A., Duffy, J., and Hawley, R. H., 1987, "Measurement of the Temperature Profile During Shear Band Formation in Steels Deforming at High Strain Rates," J. Mech. Phys. Solids, 35(3), pp. 283–301.
[12] Lee, Y. K., 1989, "Conditions for Shear Banding and Material Instability in Finite Elastoplastic Deformation," Int. J. Plast., 5(3), pp. 197–226.
[13] Latourte, F., Feinberg, Z., Mori, L., Olson, G., and Espinosa, H., 2010, "Shear and Tensile Plastic Behavior of Austenitic Steel TRIP-120 Compared With Martensistic Steel HSLA-100," Int. J. Fract., 162(1–2), pp. 187–204.
[14] Rittel, D., Lee, S., and Ravichandran, G., 2002, "A Shear-Compression Specimen for Large Strain Testing," Exp. Mech., 42(1), pp. 58–64.
[15] Dorogoy, A., and Rittel, D., 2005, "Numerical Validation of the Shear Compression Specimen. Part 1: Quasi-Static Large Strain Testing," Exp. Mech., 45(2), pp. 167–177.
[16] Dorogoy, A., and Rittel, D., 2005, "Numerical Validation of the Shear Compression Specimen. Part 2: Dynamic Large Strain Testing," Exp. Mech., 45(2), pp. 178–185.
[17] Vural, M., Rittel, D., and Ravichandran, G., 2003, "Large Strain Mechanical Behavior of 1018 Cold-Rolled Steel Over a Wide Range of Strain Rates," Metall. Mater. Trans. A, 34(12), pp. 2873–2885.
[18] Rittel, D., Wang, Z. G., and Dorogoy, A., 2008, "Geometrical Imperfection and Adiabatic Shear Banding," Int. J. Impact Eng., 35(11), pp. 1280–1292.
[19] Clifton, R. J., 1985, "Stress Wave Experiments in Plasticity," Int. J. Plast., 1(4), pp. 289–302.
[20] Kolsky, H., 1949, "An Investigation of the Mechanical Properties of Materials at Very High Rates of Loading," Proc. Phys. Soc. London, Sect. B, 62(11), pp. 676–700.
[21] Hodowany, J., 1997, "On the Conversion of Plastic Work Into Heat," Ph.D. thesis, California Institute of Technology, Pasadena, CA.
[22] Rittel, D., Bhattacharyya, A., Poon, B., Zhao, J., and Ravichandran, G., 2007, "Thermomechanical Characterization of Pure Polycrystalline Tantalum," Mater. Sci. Eng. A, 447(1–2), pp. 65–70.
[23] Rittel, D., Ravichandran, G., and Lee, S., 2002, "Large Strain Constitutive Behavior of OFHC Copper Over a Wide Range of Strain Rates Using the Shear Compression Specimen," Mech. Mater., 34(10), pp. 627–642.
[24] Meyers, M. A., 1994, Dynamic Behavior of Materials, John Wiley & Sons, Hoboken.

[25] Clough, R. B., Webb, S. C., and Armstrong, R. W., 2003, "Dynamic Hardness Measurements Using a Dropped Ball: With Application to 1018 Steel," Mater. Sci. Eng. A, **360**, pp. 396–407.

[26] Johnson, G. J., and Cook, W. H., 1983, "A Constitutive Model and Data for Metals Subjected to Large Strains, High Strain Rates and High Temperatures," *Proceedings of the Seventh International Symposium on Ballistics*, The Hague, pp. 541–547.

[27] Sung, J. H., Kim, J. H., and Wagoner, R. H., 2010, "A Plastic Constitutive Equation Incorporating Strain, Strain-Rate and Temperature," Int. J. Plast., **26**(12), pp. 1746–1771.

[28] Armstrong, R. W., and Walley S. M., 2008, "High Strain Rate Properties of Metals and Alloys," Int. Mater. Rev., **53**(3), pp. 105–128.

[29] Drucker, D. C., 1951, "A Definition of Stable Inelastic Material," *Proceedings of the First U.S. National Congress of Applied Mechanics ASME*, Chicago, pp. 487–491.